# Inorganic Chemistry

# Bond Covalency and Oxidation State of Actinide Ions Complexed with Therapeutic Chelating Agent 3,4,3-LI(1,2-HOPO)

Morgan P. Kelley,[†] Gauthier J.-P. Deblonde,[‡] Jing Su,[†] Corwin H. Booth,[‡] Rebecca J. Abergel,[‡] Enrique R. Batista,[*,†] and Ping Yang[*,†]

[†]Theoretical Division, Los Alamos National Laboratory, Los Alamos, New Mexico 87544, United States

[‡]Chemical Sciences Division, Lawrence Berkeley National Laboratory, Berkeley, California 94720, United States

**S** Supporting Information

**ABSTRACT:** The hydroxypyridinone ligand 3,4,3-LI(1,2-HOPO) is a promising agent for biological decorporation of radionuclides, and allows spectroscopic detection of many lanthanide (Ln) and actinide (An) species via sensitized luminescence. Despite the manifest uses of this ligand, the structural and thermodynamic properties of its complexes across the An series remain understudied. Theoretical investigations of the binding of An(III) and An(IV) ions, from actinium to einsteinium, by the 3,4,3-LI(1,2-HOPO) ligand, as well as experimental extended X-ray absorption fine structure (EXAFS) studies on the trivalent americium, curium, and californium complexes were employed to address the resulting structures, thermodynamic parameters, redox properties, and corresponding electronic configurations. An(IV) ions were found to form much stronger complexes than An(III) ions, consistent with experimental measurements. Complexation of both An(III) and An(IV) ions generally becomes more favorable for heavier actinides, reflecting increased energy degeneracy driven covalency and concomitant orbital mixing between the 5f orbitals of the An ions and the $\pi$ orbitals of the ligand. Notably, the ability of this ligand to either accept or donate electron density as needed from its pyridine rings is found to be key to its extraordinary stability across the actinide series.

Covalency in Actinide Complexes of Decorporation Ligand 3,4,3-LI(1,2-HOPO)
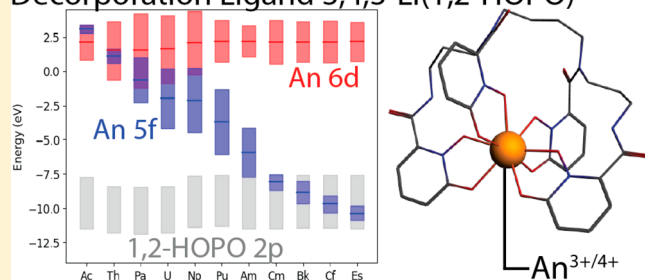
## ■ INTRODUCTION

Radiological contamination incidents can result in widespread radiation exposure to both local and remote regions. Representing an extreme recent example, the 2011 Fukushima Daiichi Nuclear Power Plant accident resulted in the dispersal of several radionuclides across a wide area, including portions of the continental U.S.[1] Actinide (An) and lanthanide (Ln) fission product species are likely to be major components of such contamination events, and it is therefore necessary to thoroughly understand and study the behavior of these ions in environmental and biological systems.[2]

Internal contamination of human populations in the event of a radiological incident, whether accidental or intentional, is of critical concern. Once internalized, An ions transit rapidly throughout the bloodstream and are primarily deposited in the liver and bones (uranium is an exception and preferentially deposits in the kidneys rather than in the liver), from which elimination occurs very slowly.[3,4] Uptake and deposition of these ions present severe health risks due to both their radiological and chemical toxicities.[3] Medical treatments for removal of An ions from the body are deemed essential in limiting radiation exposure. Decorporation is primarily done through chelation therapy, in which a ligand is introduced into the body to complex the ions; the ions are then expelled from the body concurrently with the ligand in either the urine or

feces. Stemming from the similar charge to ionic radius ratios and coordination behaviors of Fe(III) and Pu(IV),[5] a promising class of compounds for the purpose of decorporation are the siderophore-inspired[6] multidentate hydroxypyridinonate (HOPO) ligands, which have a peerless affinity for the An ions.[7]

HOPO chelators coordinate isotopes of the An and Ln series exceptionally well both *in vitro* and *in vivo*, and have been shown to be effective decorporation agents in multiple animal models.[8−19] Two hydroxypyridinonate ligands have undergone preclinical development as potential therapeutic agents for actinide decorporation: the tetradentate chelator 5-LIO(Me-3,2-HOPO) and the octadentate chelator 3,4,3-LI(1,2-HOPO),[17] with the latter now entering a first-in-human clinical phase. Both of these ligands have been shown to be significantly more effective An decorporation agents than the only approved and used drug so far: the diethylenetriaminepentaacetic acid (DTPA).[17] Further, HOPO ligands have potentially a wide array of additional medical uses. A HOPO ligand has been proposed as a Gd(III) chelator for use as a contrast agent in magnetic resonance imaging,[20−23] and HOPO ligands have been suggested as complexants in radiopharmaceutical treat-

ments using $^{89}$Zr(IV), $^{225}$Ac(III), and $^{227}$Th(IV).[24,25] In addition to their manifest medical utility, HOPO ligands have analytical uses. 3,4,3-LI(1,2-HOPO) is known to sensitize the luminescence of several Ln(III), An(III), and An(IV) cations through the antenna effect,[26−33] allowing these systems to be characterized spectroscopically and opening up a range of innovative applications including fluorescence-based bioassays.[31,32,34−38] A recent report has shown 3,4,3-LI(1,2-HOPO) capable of stabilizing Bk in the +4 oxidation state—the first stable Bk(IV) species observed in solution—a development potentially leading to novel Bk separation and purification techniques.[33]

Despite the promising applications of HOPO ligands, a number of gaps in knowledge of their fundamental chemistry remain. Thermodynamic measurements have been performed with 3,4,3-LI(1,2-HOPO) across the Ln(III) series, and with Am(III), Cm(III), Ce(IV), Th(IV), and Pu(IV).[8−11,39,40] However, the stability constants of M(IV)−3,4,3-LI(1,2-HOPO) complexes have proven more difficult to measure, as they exceed the stability of any known ligand with these ions.[8,9,39] Furthermore, while the primary uses of HOPO ligands are in biological systems, thermodynamic measurements have necessarily been performed *in vitro*, and current knowledge of *in vivo* complex stability is derived solely from the decorporation profiles of the ions.[8,11−17] *In vivo*, the oxidation state of the Ln and An ions is uncertain upon complexation, as there is some evidence suggesting HOPO may induce the oxidation or reduction of the metal ions.[9,39,41] Finally, the structure and bonding of the 3,4,3-LI(1,2-HOPO) complexes have not yet been fully investigated. To our knowledge, only the single-crystal X-ray structure of Eu(III) complexed with 3,4,3-LI(1,2-HOPO) has been obtained,[31] while structures of Sm(III), Eu(III), Gd(III), Am(III), Cm(III), and Cf(III) complexes have been determined when bound to the protein siderocalin (Scn).[33,42] Currently, the only reported structure for a tetravalent metal ion complex of 3,4,3-LI(1,2-HOPO) is with Zr(IV).[43] Due, in part, to the large amount of material needed, no crystal structure of a free (non-protein-bound) An-3,4,3-LI(1,2-HOPO) complex has ever been reported. Some of the actinide contaminants potentially requiring decorporation have had neither structural nor thermodynamic measurements performed; this gap in knowledge can be addressed well with computational studies. Furthermore, the underlying causes of complexation, including the role of covalency in the An−ligand interaction, can be investigated via electronic structure calculations.

The present work uses density functional theory (DFT) combined with extended X-ray absorption fine structure (EXAFS) measurements to advance our current understanding of An-3,4,3-LI(1,2-HOPO) complexes. Their structure, thermodynamics, electronic structures, and redox properties are investigated across the An series up to Es, with both formally An(III) and An(IV) ions. The similarity of 3,4,3-LI(1,2-HOPO) to other biological complexants and the wealth of excellent experimental information on this system ensures that a fundamental understanding of An-3,4,3-LI(1,2-HOPO) complexation will have applications beyond this single ligand, and presents an opportunity to study trends in An-ligand binding across the actinide series that can inform future work developing An complexants.

## ■ RESULTS AND DISCUSSION

**Structure.** The 3,4,3-LI(1,2-HOPO) ligand (Scheme 1; henceforth referred to as "HOPO" to simplify the notation)

**Scheme 1. Structure of 3,4,3-LI(1,2-HOPO)**
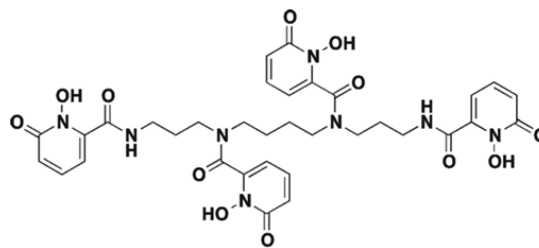


incorporates four hydroxypyridinone 1,2-HOPO groups linked through a polyamine scaffold, and is capable of forming octadentate complexes with An ions, occupying all—or nearly all—of the first coordination shell of the ion. Ions are bound through the oxygen atoms within the 1,2-HOPO units, O(C) and O(N) (the carbonyl and hydroxyl groups within the hydroxamate, respectively). When fully deprotonated, HOPO carries four negative charges.

Density functional theory has frequently been applied to complicated An systems with good results,[44−52] and has previously been used to study HOPO complexes. Daumann et al. used DFT to optimize the structure of the [Eu(HOPO)]$^−$ complex, resulting in a gas phase geometry consistent with the crystal structure and a calculated UV−vis spectra matching experimental measurements.[31] DFT was also used by Deri et al. to study the [Zr(HOPO)]$^0$ complex, using their computational results to direct the synthesis of improved ligands for Zr(IV) complexation.[25] Several studies have used time dependent DFT to study lanthanide luminescence sensitization by ligands containing the 1,2-HOPO unit,[26,40,53−55] in addition to calculations on Am and Cm.[40] These results suggest that DFT is a useful method for studying the metal−HOPO system.

Figure 1 shows the ion-oxygen distances in structures optimized in the gas phase and utilizing implicit solvation models (polarizable continuum model) with the dielectric constant of water and that of a protein environment, as the HOPO ligand is frequently used *in vivo*. The results presented in Figure 1 show excellent agreement with available experimental crystal structures.[15,24,31,32,42,56−59] The optimized aqueous [Eu(HOPO)]$^−$ complex has an average Eu−O distance of 2.45 ± 0.01 Å, within uncertainty of the experimentally determined average of 2.40 ± 0.04 Å.[31] Several other experimental studies have determined coordination structures of individual 1,2-HOPO units (without the polyamine scaffold) in tetrakis-bidentate complexes.[57−59] The average Pu(IV)−O distances in these structures are 2.33 ± 0.02 Å, compared to 2.36 ± 0.02 Å for the calculated distances (Figure 1). Experimentally determined Fe(III)−O, Ce(IV)−O, and Th(IV)−O distances in the 1,2-HOPO complexes are likewise consistent with our calculations of 3,4,3-LI(1,2-HOPO) complexes.

The An−O(C) and An−O(N) distances are generally not statistically distinct in measured crystal structures, as is generally the case in our results. Furthermore, the structure of the aqueous [Zr(HOPO)]$^0$ complex matches nearly exactly that of the B3LYP optimized structure of Deri et al., who calculated average Zr−O(C) and Zr−O(N) distances of 2.22 ±
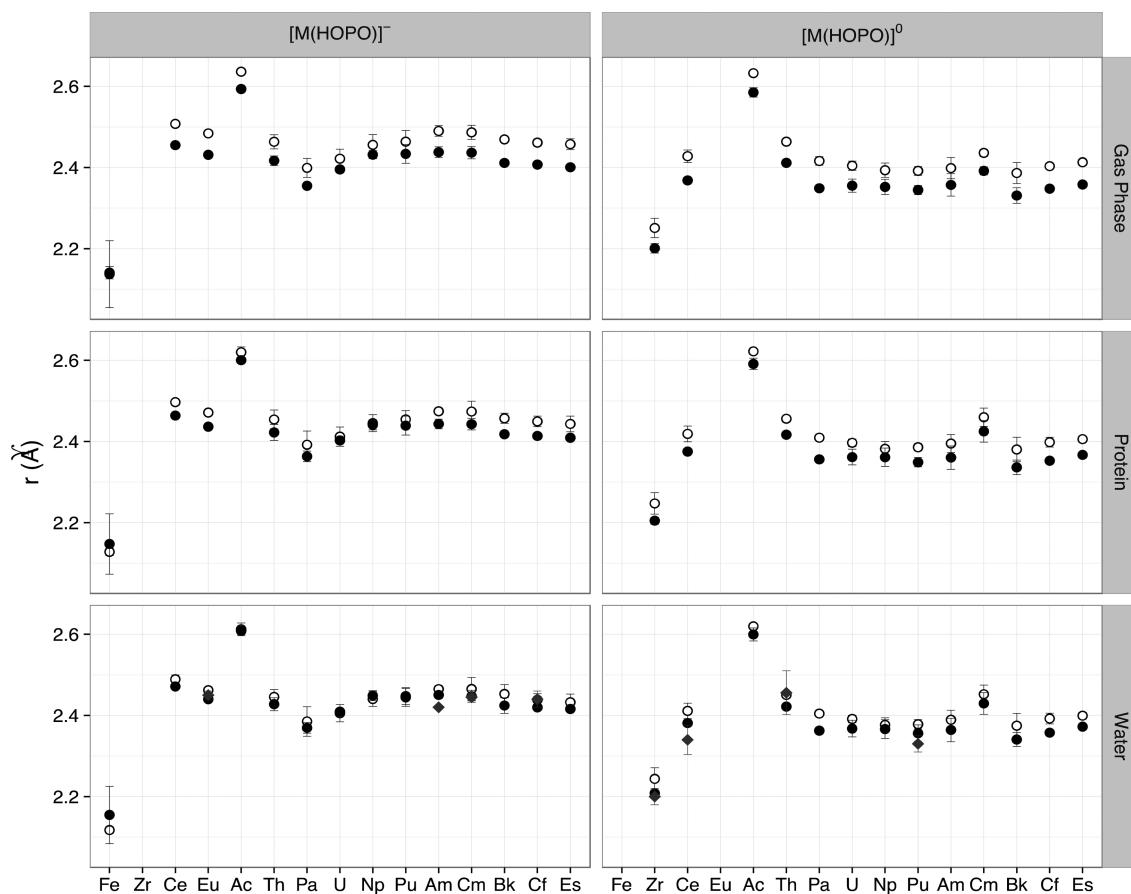
**Figure 1.** Ion-oxygen distances, M−O(N) (○) and M−O(C) (●), in $[M(HOPO)]^-$ and $[M(HOPO)]^0$ complexes. Experimental M−O distances (red ◆) are included when available, for Eu, Zr (crystal structures),[31,43] Ce, Th, and Pu (crystal structures from the bidentate 1,2-HOPO ligand),[56,58] and Am, Cm, and Cf (EXAFS data from this work). Error bars depict the standard deviation of ion−oxygen distances in the complex or the experimental uncertainty.

0.05 and 2.27 ± 0.04 Å, respectively, compared with 2.208 ± 0.007 Å and 2.24 ± 0.03 Å in the present study.[25] Sturzbecher-Hoehne et al. optimized structures of $[Eu(HOPO)]^-$, $[Am(HOPO)]^-$, and $[Cm(HOPO)]^-$ in the gas phase using the PBE functional. Ion-oxygen distances are nearly identical to the gas phase structures presented here for all three ions.[40]

**EXAFS Measurements.** To further verify the DFT/PBE structures, EXAFS measurements were performed on the later actinides, as no experimental structural data were available in the literature for comparison. Usable EXAFS data were obtained on HOPO complexes formed *in situ* with Am, Cm, and Cf (the amount of Bk material available for these experiments was too limiting). The data quality is best for the Am and Cm spectra, allowing for sharper spectra and a confident comparison to the fit model. The $[Cf(HOPO)]^-$ data are of lesser quality (only ~3 μg available for measurements), limiting the range in wave vector k (Figure 2, top). Though details of the fitting models are provided in the Supporting Information, we describe several important features here. The fitting model for the Am and Cm data is derived from a simplification of the $M^{3+}$ calculations described above. In particular, each scattering shell is modeled by a single atom pair, which is multiplied by the nominal coordination number and Gaussian broadened by a Debye−Waller factors, $\sigma^2$, to account for any distribution of such bonds, as well as thermal broadening. This assumption, namely that the distribution of bonds is narrow enough that a Gaussian will describe the

structure adequately, can be considered justified by the relatively small values of $\sigma^2$ (less than 0.02 Å$^2$ for all shells) and the overall good quality of the fits. In addition, the second shell near 3.3 Å in the calculation includes both 4 C and 4 N neighbors. Since these species are virtually indistinguishable in this measurement, their bond lengths are constrained together and their Debye−Waller factors, $\sigma^2$, set equal, so any differences in the An−C and An−N distributions for this shell are reflected in the average $\sigma^2$. In addition, the Cm data require an additional shell, corresponding to a bond length near 3.0 Å (98% confidence level[60]). Since $Cm^{3+}$ luminescence lifetime measurements indicate the presence of inner-sphere water,[10] we tentatively ascribe this peak to an oxygen scatterer, although we note the long bond length and large error in $\sigma^2$, which may be a consequence of a dynamic coordination. We also find such a peak improves the fits to the $[Am(HOPO)]^-$ data, although with less confidence (75% confidence level). We emphasize that the presence of this peak in the spectrum has no effect on the bond lengths reported below.

To further consider inner-sphere water coordination, we used a number of different strategies to optimize the calculated $[Am(HOPO)(H_2O)]^-$ structure, but none was successful. In the absence of constraints, the added water molecule moved away from the ion to a distance of approximately 4.3 Å, where it formed two hydrogen bonds with HOPO oxygen atoms coordinating to the Am ion. It is possible that solution dynamic effects would establish an equilibrium in which a water
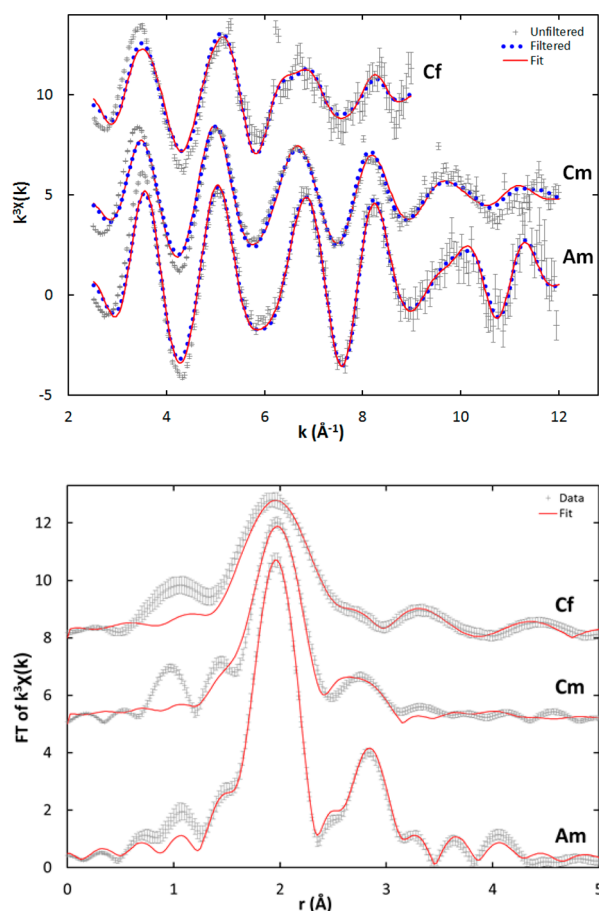
C

**Figure 2.** EXAFS data and fit results from the An $L_{III}$ edge of $[An(III)(HOPO)]^-$ (An = Am, Cm, or Cf). The upper panel shows the results in *k*-space. The raw (unfiltered) data reveal error bars estimated by the reproducibility of 16 (Am, Cm) to 21 (Cf) averaged traces. The bottom panel shows the data and fit are transformed from 2.5 to 12.0 Å$^{-1}$ (from 2.5 to 9.0 Å$^{-1}$ for Cf) and fit between 1.5 and 4.3 Å (between 1.4 and 5.0 Å for Cf). The filtered data and fit in the top panel are back-transformed over the fit range. See Tables S3 and S4 for fit details.

molecule is sometimes in the first coordination shell of the ion and sometimes in the second coordination shell. To fully investigate this question, it is necessary to include both explicit solvents and dynamic simulation which is beyond the scope of this work.

Other than the exceptions described above, the fit model obtained from calculated structures describes the data well (Figure 2). Generally speaking, the EXAFS data are consistent with the HOPO complex structure calculations for the nearest neighbor M(III)−O pair distances with the largest deviation occurring with $[Am(HOPO)]^-$. In addition, the Cf−C/N average bond length differs from calculation, but the calculation also shows a broad distribution width for the 8 bonds in this shell. Table 1 compares the EXAFS bond length results to those derived from the DFT calculations for the first two shells. Further details of the methods and results are available in Supporting Information (pp S11−S15).

**DFT Structure.** The ions shown in Figure 1 maintain a coordination number of 8, with the exception of the 7 coordinate $Fe^{3+}$, in which one of the O(N) groups is rotated away from the ion with an $Fe^{3+}$−O distance of 3.6 Å. This is consistent with the ionic radius (IR) of $Fe^{3+}$, 0.78 Å, which is

**Table 1. Comparison between Measured (EXAFS) and Calculated $M^{3+}$ Nearest-Neighbor Bond Lengths**

| number | bond type | $R_{EXAFS}$ (Å)[a] | $R_{DFT}$ (Å)[b] |
|---|---|---|---|
| 8 | Am−O | 2.420(6) | 2.46(1) |
| 8 | Am−C/N | 3.292(7) | 3.33(3) |
| 8 | Cm−O | 2.444(6) | 2.46(2) |
| 8 | Cm−C/N | 3.24(2) | 3.31(3) |
| 8 | Cf−O | 2.45(2) | 2.43(2) |
| 8 | Cf−C/N | 3.54(10) | 3.29(3) |

[a]Values in parentheses indicate fit error. [b]Values in parentheses indicate standard deviation of bond length distribution.

significantly smaller than the next smallest ion in Figure 1, $Zr^{4+}$ (IR = 0.84 Å).[61] Calculations performed on main group cations, $K^+$, $Ca^{2+}$, and $Al^{3+}$, revealed similar trends. $Al^{3+}$ (IR = 0.535 Å)[61] has a coordination number of 6, with two O(N) groups rotating away from the ion. $Ca^{2+}$ is much larger (IR = 1.12 Å)[61] but has a significantly lower charge density, resulting in a loose 8 coordinate complex in which the average distance to the oxygen atoms is greater than 2.5 Å. $K^+$, with the lowest charge density and the largest ionic radius (IR = 1.38 Å)[61] of any ion examined here, forms a 6 coordinate complex. This is achieved not by rotating two oxygen atoms away, as $Al^{3+}$ does to accommodate its smaller ionic radius, but by the disengagement of an entire 1,2-HOPO unit from the ion. This results in a very loose 6-coordinate complex with average coordinated $K^+$−O distances greater than 2.8 Å. The structural deformities seen here for other ions commonly found in biological systems could represent an advantage for An complexation, minimizing competition with ions naturally present in the bloodstream, as the size and conformation of the complex is likely to impact its interaction with proteins like Scn,[42] therefore leading to selectivity of An ions. Some of these complexes are illustrated in Figure 3. Additionally, the structures of the $Al^{3+}$ and $Fe^{3+}$


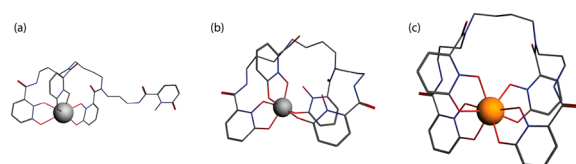
**Figure 3.** Ion-HOPO structures for complexes with (a) $K^+$, (b) $Al^{3+}$, and (c) $Cm^{3+}$. Metal ions are represented by spheres, HOPO$^{4-}$ atoms by sticks; red = oxygen, blue = nitrogen, gray = carbon. Hydrogen atoms omitted for clarity. Structure c is representative of all Ln and An complexes, which can be found in the Supporting Information, along with coordinates for all structures.

complexes, with the O(N) groups rotating away to accommodate the smaller ions, imply that the M−O(N) bonds are slightly weaker than the M−O(C) bonds.

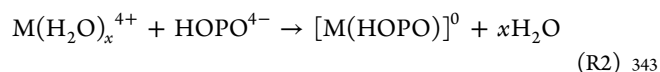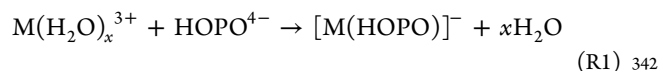The $[An(HOPO)]^-$ complexes show a fairly small but consistent increase in An−O distances starting with Th and leveling off around Am. While this is the opposite trend expected from the decrease in ionic radii across the series due to the contraction of the 5f orbitals, it can be understood via the electronic structure of the earlier An ions, many of which strongly disfavor the An(III) oxidation state. These ions are essentially oxidized to An(IV), matching the An−O distances of the $[An(HOPO)]^0$ complexes; this is explored in subsequent sections. $Ac^{3+}$ is significantly further from the oxygen atoms in line with its larger ionic radius and consistent with recent

EXAFS measurements showing Ac(III)−H$_2$O and Ac$^{3+}$−Cl distances to be 0.1−0.2 Å greater than corresponding Am$^{3+}$ complexes.[44,62] [An(HOPO)]$^0$ complexes behave more predictably, with An(IV)−O distances initially decreasing as the ionic radius decreases and then remaining nearly constant beyond U(IV). [Cm(HOPO)]$^0$ is a notable exception to this trend, having an increase in An−O distance inconsistent with the rest of the series. The reasons behind this discrepancy will be covered in the discussion of electronic structure.

There are only minor differences—like the convergence of the M−O(N) and M−O(C) distances in water—between the structures optimized in the gas phase, the protein-like environment, and water using the implicit solvation model employed here, as shown in Figure 1. Upon binding by a protein, it is important to note that the HOPO ligand is flexible and therefore the complex structures can be influenced by strong explicit interactions occurring between the metal complex and the protein. Hence the structures of complexes identified in proteins may show larger deviation from the data in this report.

**Thermodynamics.** The free energies of complexation by the HOPO$^{4-}$ ligand were calculated at the DFT/PBE0 level to compare with experimental thermodynamic measurements of the stability constants across the An series. These computed free energies between the hydrated ions (using both an explicit first solvation shell of water and the implicit polarizable continuum model) and HOPO$^{4-}$ Reactions R1 and R2 are shown in Figure 4. As with the ion-oxygen distances presented

**Figure 4.** Free energy ($\Delta G$) of complexation between the hydrated ions and the HOPO$^{4-}$ ligand in implicit water solvent.

above, the trends between the gas phase calculations, the calculations including the implicit water solvent, and those with a protein-like solvent are similar, most likely because the complex is not very polarizable (see Supporting Information, Figure S6 for thermodynamic calculations in the two solvation environments and the gas phase using the bare ions); therefore, only those using implicit water solvation are shown in Figure 4. The calculated $\Delta G$ of complexation for the M(IV) ions is significantly lower than that of the M(III) ions. This matches well with experimental thermodynamic studies (Table 2),

**Table 2. Experimentally Measured Stability Constants for Relevant Ln and An ions with HOPO.[a]**

| M$^{3+}$ | log($\beta_{101}$) | M$^{4+}$ | log($\beta_{101}$) |
|---|---|---|---|
| Ce$^{3+}$ | 17.4(5)[39] | Ce$^{4+}$ | 41.5(5)[39,42] |
| Eu$^{3+}$ | 20.2(2)[11,28] | Th$^{4+}$ | 40.1(5)[9,39] |
| Am$^{3+}$ | 20.4(2)[40] | Pu$^{4+}$ | 43.5(7)[9] |
| Cm$^{3+}$ | 21.8(4)[10] | Bk$^{4+}$ | 44.7[b,33] |

[a]Superscripts indicate reference from which data is cited. [b]Estimation based on a linear ionic radius correlation.

which have measured log($\beta_{101}$) values for HOPO with M(IV) ions nearly double those of M(III) complexes.[9,39] For example, the log($\beta_{101}$) for Ce$^{3+}$ is 17.4(5) while that for Ce$^{4+}$ is 41.5(5), corresponding to an energy difference of approximately 33 kcal/mol.[39] This is the same order of magnitude as the difference in Ce$^{3+}$ vs Ce$^{4+}$ calculated here, despite these calculations considering only the solvated ion within a polarizable continuum without counterions or other aspects of solvation.

$$M(H_2O)_x^{3+} + HOPO^{4-} \rightarrow [M(HOPO)]^- + xH_2O$$
(R1)

$$M(H_2O)_x^{4+} + HOPO^{4-} \rightarrow [M(HOPO)]^0 + xH_2O$$
(R2)

The above reactions denote the number of water molecules as "$x$", with $x = 6$ for Fe and $x = 9$ for all other ions. While the assumption of $x = 9$ is confirmed for the two Ln and the early An ions, later An ions have experimentally debated hydration numbers between eight and nine.[51,63−65] Precise determination of the number of water molecules within the first solvation shell of An ions is a challenging computational problem[49,50,66,67] beyond the scope of the current work. Additionally, the difference in complexation energy between a hydration number of eight or nine amounts only to the order of 3−4 kcal/mol, which is small enough to have no impact on conclusions concerning the complexation energy across the An series despite potential changes in coordination number. Fe$^{3+}$ has a hydration number of only six, with a high spin ground state for both the hydrated ion and the Fe(HOPO)$^-$ complex.

The left panel of Figure 4 depicts the Gibbs free energy ($\Delta G$) of reaction R1, where An(HOPO)$^-$ complexes have a presumed oxidation state of + III at the metal center. Reassuringly, the difference between the two trivalent Ln ions calculated here, Ce and Eu, matches experiments showing an increase in stability constants across the Ln series.[11] Complexation of the early An(III) ions is very favorable, becoming less so as the series is traversed. These early actinides—Th, Pa, and U—readily form An(IV) complexes instead of An(III) species, and the comparative favorability of complexation is due to electron donation to the HOPO stabilizing the ion. The binding energy does not significantly change after Cm$^{3+}$. Formation of the [Ac(HOPO)]$^-$ complex is less favorable than other An complexes, in line with the increased ionic radius and Ac−O distances described in the preceding section. The cause behind this decrease requires a discussion of the electronic structures of the complexes, and is provided in greater detail in the Electronic Structure section.

Formation of the [M(HOPO)]$^0$ complexes (right panel of Figure 4; reaction R2) shows $\Delta G$ of complexation for the formally An(IV) ions, which is significantly more favorable than the formally An(III) complexation of HOPO, consistent with experimental observations.[9] Complexation energy becomes more favorable as the series is traversed, but unlike the trend observed for the An(III) ions, this starts near the beginning of the series with Th. The trend is not consistent across the series, however, with Bk(IV) complexation becoming less favorable than Cm(IV). Additionally, the behavior of Ac, which changes based on the oxidation state of the ion, requires some explanation. The formation of the [Ac(HOPO)]$^-$ complex is unfavorable compared to the rest of the An series, an unsurprising observation given the significantly longer Ac−O bond lengths. Formation of the [Ac(HOPO)]$^0$ complex,
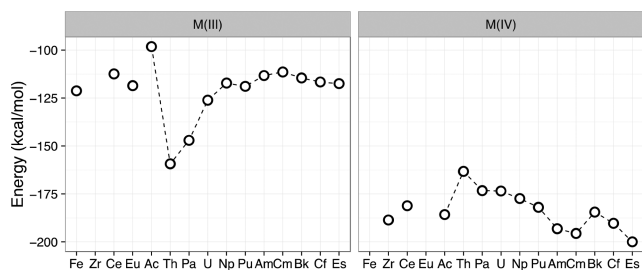
however, is more favorable compared to its neighbors in the early part of the series— exactly the opposite behavior expected from the geometry. To explain this behavior and other observations mentioned above, it is necessary to delve deeper into the electronic structure of the An-HOPO complexes.

**Electronic Structure.** Charge donation from the ligand to the ion occurs primarily into the 6d orbitals of the metal ion in [An(HOPO)]$^-$ complexes, with 5f participation increasing and 6d decreasing slightly across the actinide series up to Am (Figure 5). An exception to this is Ac, which resembles the later
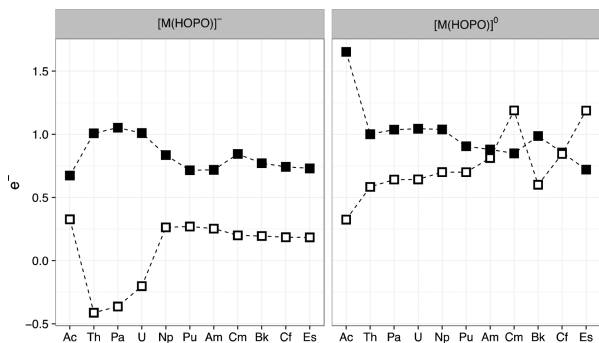
**Figure 5.** Electron donation into the valence d (■) and f (□) orbitals (6d/5f for An ions—note that a single electron is donated into the 5d orbital of Ac in the [Ac(HOPO)]$^0$ complex). The change in population (Δd and Δf; actual populations minus the formally expected An(III) or An(IV) population) is plotted here.

actinides despite its position at the beginning of the series. There is also a slight decrease in donation into the 5f between Am and Cm, possibly due to the fact that Cm$^{3+}$ is 5f$^7$ and adding an additional electron into the half-filled 5f shell is less favorable than adding into the 6d. The dual participation of the 5f and 6d orbitals matches recent experimental and theoretical studies showing participation of both the f and d orbitals in uranium complexation,[68] in addition to theoretical work on solid state and molecular structures across the An series.[46,69,70] It is important to note that it is not the absolute values of the Mulliken populations shown in Figure 5 that are important to our analyses here, but rather the trends between the An ions. The oxidation state of the metal center is better described using spin density, as in Figures 6 and 7; we note that calculated $S^2$ values are uniformly within 0.15 of the expectation value.

An interesting feature of the 6d and 5f populations in the [An(HOPO)]$^-$ complexes (Figure 5) is that Th, Pa, and U have a decrease in their 5f populations upon complexation (Δ5f < 0). This is reflective of the fact that all three of these ions are more stable as An(IV) species than An(III), and when these
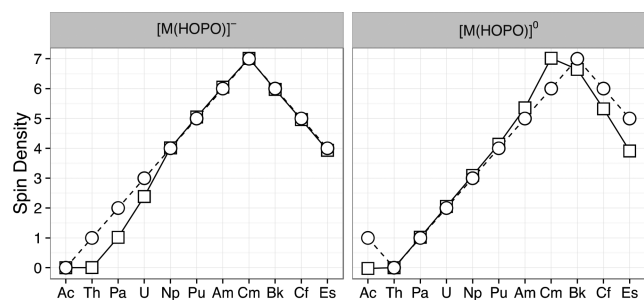
**Figure 6.** Actual (□) and formal (○) spin densities on the An ions in the [An(HOPO)]$^-$ and [An(HOPO)]$^0$ complexes.
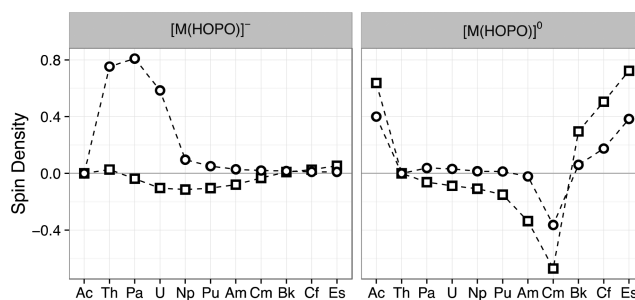
**Figure 7.** Total spin densities on the complexing 1,2-HOPO units of the HOPO$^{4-}$ molecule, grouped into total oxygen (□) and total pyridine (○) contributions.

formally An(III) ions are complexed by the HOPO$^{4-}$ ligand they are oxidized, giving up spin density to the ligand. Figure 6 shows that the actual spin density of Th, Pa, and U in the [An(HOPO)]$^-$ complexes is significantly lower than their formal spin densities as An(III) ions. The surrendered spin density moves from the ions into the HOPO$^{4-}$ ligand, where it is taken into the pyridine rings of two of four coordinating 1,2-HOPO units (Figure 7). The spin density in the pyridine ring increases, making up for the decrease in spin density on the ion (a breakdown of Figure 7 into different groups within each 1,2-HOPO unit can be found in the Supporting Information, Figure S5). Despite the oxidation of these ions, significant electron donation to the 6d orbitals from the ligand still occurs, making this exchange 5f-to-ligand back bonding. This has the effect of stabilizing the ion, resulting in the favorable complexation energy observed in Figure 4. It is clear that the ability of the pyridine ring to take electron density from the metal center contributes to the stability of the [An(HOPO)]$^-$ complexes with the early actinides. Introducing an even better electron-withdrawing group could be a path toward creating better chelators for the low oxidation states of early actinides.

Actinide ions in the [An(HOPO)]$^0$ complexes have levels of electron donation into their 6d orbitals comparable to those in the [An(HOPO)]$^-$ complexes, but significantly greater donation into the 5f orbitals. Electron donation into the 5f orbitals (relative to the formal An(IV) expectation) increases across the series, a trend briefly reversed at Bk. This is because unlike other late actinides, Bk maintains a + IV oxidation state, as demonstrated by the spin density. The trend of increasing 5f participation continues in Cf and Es.

The unexpected increase in the Cm(IV)−O distances relative to the other An (HOPO)$^0$ complexes (Figure 1) can be explained by examining Figure 6 and Figure 7. Our observed increase in Cm−O distances matches observations from calculations on solid-state AnO$_2$ structures, that predict an increase in the lattice constant of CmO$_2$ relative to the rest of the series. This was explained by Prodan et al.[70] as being due to the electronic configuration of Cm(IV), 5f$^6$. This less stable electron configuration leads Cm(IV) to borrow α spin density from the coordinating oxygen atoms in order to approach the stability of the 5f$^7$ subshell, resulting in a spin density on the Cm atom between the formal Cm(III) and Cm(IV). The spin density on the Cm atom in the [Cm(HOPO)]$^0$ complex is nearly 7, indicating that the Cm(IV) has been reduced by HOPO$^{4-}$ to Cm(III). Unlike the solid CmO$_2$, the 1,2-HOPO units have other atoms aside from oxygen to donate spin density; an increase in spin density on the pyridine ring, in addition to the coordinating oxygen atoms, is observed. We

**Table 3. Calculated Free Energy ($\Delta G$) of Oxidation for the $[An(HOPO)]^-$ Complexes to $[An(HOPO)]^0$, in Water Relative to Ferrocene (eV)**

|            | Ac   | Th    | Pa    | U     | Np    | Pu    | Am   | Cm   | Bk   | Cf   | Es   |
|------------|------|-------|-------|-------|-------|-------|------|------|------|------|------|
| $\Delta G$ | 1.19 | −1.76 | −1.95 | −1.99 | −1.01 | −0.20 | 0.72 | 1.23 | 0.01 | 1.32 | 1.24 |

note that the majority of the donated spin density comes from the oxygen atoms rather than the pyridine ring, though both groups participate. Increasing the electron donation ability of the coordinating atoms could result in a stronger complex. This trend continues for the later actinides, which are also essentially reduced to An(III). However, with an already half-filled 5f subshell, the actinides after Cm take $\beta$ spin from the 1,2-HOPO units, resulting in a spin density lower than what would be expected for a formally An(IV) ion and a corresponding increase in spin density on the HOPO$^{4-}$.

The ability of the HOPO$^{4-}$ ligand to allow coordinating actinide ions to attain their most stable oxidation states by either accepting or donating electron density also explains the behavior of Ac, where the formation of the $[Ac(HOPO)]^0$ complex was significantly more favorable than any other complex, counter to expectations from trends in the optimized geometries and inconsistent with the formation of the $[Ac(HOPO)]^-$ complex. Ac(IV) has a formal $6p^5 5f^0$ electron configuration, which is very unstable. Ac(IV) is, as expected, quite easily reduced to Ac(III) by the ligand, completing the 6p shell to become $6p^6 5f^0$. The spin density on Ac(IV) is zero, reduced from a formal spin density of 1 (Figure 6), which is compensated by an increase in spin density on the HOPO$^{4-}$ ligand (Figure 7). Spin density from both coordinating oxygen atoms and the pyridine ring of all four 1,2-HOPO units is taken to reduce Ac(IV). Since the Ac(IV) ion is unstable, complexation with HOPO is more favorable due not to the increased stability of the complex but rather the instability of the Ac(IV) ion; by reducing Ac(IV) and filling the 6p shell, the HOPO stabilizes the Ac ion as Ac(III), resolving the previously anomalous trend in Figure 4.

Table 3 shows the free energy of the oxidation potentials of the $[M(HOPO)]^-$ complexes to $[M(HOPO)]^0$, relative to ferrocene/ferrocenium (Fc$^0$/Fc$^+$; $\Delta G$ for the ferrocene redox couple was calculated as 4.52 eV). The $[Ce(HOPO)]^-$/$[Ce(HOPO)]^0$ redox couple has been measured experimentally[39] as −0.3(1) eV when adjusted relative to Fc$^0$/Fc$^+$; this is a good match with the −0.55 eV value calculated here. The difference between the calculated result and experimental measurements is within the uncertainty of the applied method.[71] The redox potentials of all early actinide complexes, up to Pu, are negative compared to ferrocene (with the exception of Ac), while all later actinide complexes have positive redox potentials relative to the Fc$^0$/Fc$^+$ couple. The complexes with ions having more stable An(IV) oxidation states (i.e., Th, Pa, and U) are significantly easier to oxidize to $[M(HOPO)]^0$; this is because in the $[M(HOPO)]^-$ complexes, the metal centers are already in oxidation state IV resulting in additional electron density residing on the HOPO ligand, leading to the ease of removal of the electron during the oxidation process and the negative oxidation potential. For Np and Pu complexes, it is the metal center being oxidized. In contrast, the late actinide ions in $[M(HOPO)]^0$ mentioned above (Cm, Cf, Es) are reduced to An(III) during complexation with HOPO$^{4-}$, and are the least likely to form $[M(HOPO)]^0$ complex. For these complexes, it is the HOPO ligand being oxidized instead of metal center. Bk is somewhat

of an exception to this trend, as the Bk center is being oxidized, with a $\Delta G$ of oxidation of only 0.01 eV, essentially the same as that of Fc$^0$/Fc$^+$ couple and contrasting with its neighbors Cm and Cf which both have values over 1 eV. Metal oxidation states are known to have some dependence on complexing ligands,[72,73] and this redox data gives further evidence of the stabilization of An(IV) ions by HOPO, recently observed by Deblonde et al. in their investigation of Bk$^{4+}$ complexation by HOPO.[33] These differences in redox potential correspond to the changes in the An spin density observed in Figure 6.

**Covalency across the An Series.** As the An series is traversed, the energy of the An 5f orbitals decreases and aligns better with that of the ligand orbitals, enhancing orbital mixing between the metal center and the ligand. This effect can be seen in Figure 8 for both the $[An(HOPO)]^-$ and $[An(HOPO)]^0$ complexes. The descending energy levels of the 5f orbitals across the An series and their corresponding increase in degeneracy with the conjugated $\pi$ orbital of the 1,2-HOPO units in the HOPO$^{4-}$ ligand yield the increase in charge donation into the 5f orbitals with the 6d orbitals maintaining a
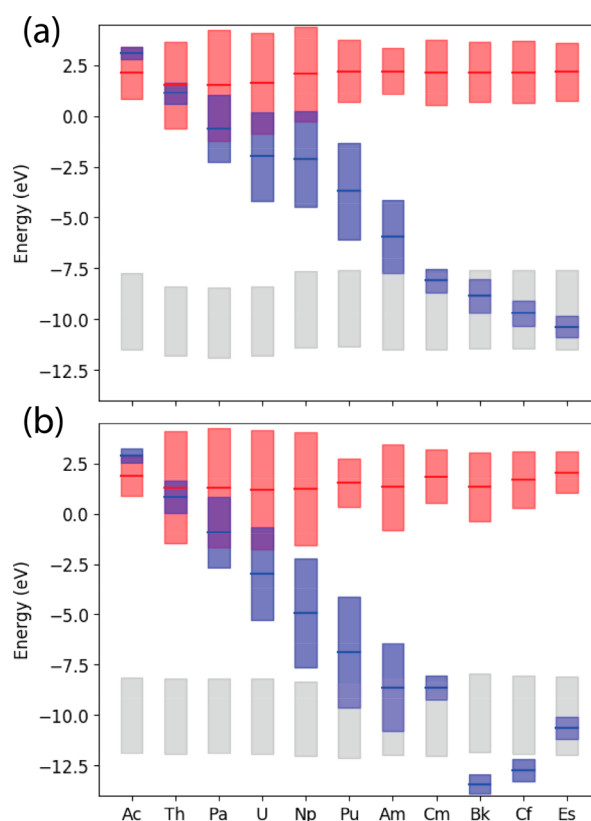


**Figure 8.** Average energy levels of the 5f (blue) and 6d (red) orbitals in the (a) $[An(HOPO)]^-$ and (b) $[An(HOPO)]^0$ complexes. The conjugated $\pi$ orbital of the 1,2-HOPO units in the HOPO$^{4-}$ ligand (which includes the pyridine ring and the coordinating oxygen atoms) are also shown for each complex (gray). Darker lines represent the average energy value of the orbitals, while the shaded regions give the standard deviation. Averages and standard deviations of the orbital energies are weighted by MO composition.

constant energy and population across the series, as observed in Figure 5. These findings across the entire An series corroborate the work of Sturzbecher-Hoehne et al., who found increased orbital overlap in the $[\text{Cm(HOPO)}]^-$ complex relative to the $[\text{Am(HOPO)}]^-$ complex, suggesting that this might be responsible for the increase in binding constant between the two actinides.[40] This decrease in An 5f energy has been observed previously in a number of different studies, including oxygen ligands in both solid state and molecular systems.[46,69,70,74,75] Comparing Figure 8, parts a and b, one notes that the change of 5f orbital energy across the series is oxidation state dependent; for example, the sudden drop in 5f energy between Cm and Bk in Figure 8b occurs because Cm is actually Cm(III) and Bk is Bk(IV) in the $[\text{An(HOPO)}]^0$ complexes. Comparing Figure 8b with solid state $\text{AnO}_2$ systems where the metal centers are all formally oxidation state IV shows that the energy degeneracy to 5f orbitals displays strong dependency to the ligand type—in the solid-state system, the 5f orbitals interact with the oxygen 2p orbitals only, while here they interact with the conjugated $\pi$ orbital formed by the oxygen of the pyridine ring.

As the An 5f orbitals become more degenerate with the $\pi$ orbital of the 1,2-HOPO units in the $\text{HOPO}^{4-}$ ligand, significant mixing between the An 5f and the ligand orbitals occurs. Until $\text{Am}^{3+}$, each $[\text{An(HOPO)}]^-$ complex has all of its occupied f molecular orbitals localized in the metal. As the series is traversed, however, the 5f orbitals become increasingly mixed with the ligand orbitals. For example, in $[\text{Bk(HOPO)}]^-$, the 5f orbitals are spread across 29 molecular orbitals, each with at least 5% f participation. A similar trend is observed in the $[\text{An(HOPO)}]^0$ complexes starting at Pu, consistent with the overall lower energy of the 5f orbitals in the $[\text{An(HOPO)}]^0$ complexes. This explains why the complexes become more stable across the latter part of the An series, despite the 6d orbitals remaining at a constant energy level. Additional data on the delocalization of the 5f orbitals, including molecular orbital diagrams, is available in the Supporting Information (Figures S1−S4). The changing energy levels of the 5f orbitals also sheds light on the unexpected break in the thermodynamic trends at Bk(IV), where an increase in $\Delta G$ of complexation (that is, $\Delta G$ becomes less negative) between Cm and Bk in $[\text{An(HOPO)}]^0$ is observed (Figure 4). This corresponds to the 5f orbitals of Bk (Bk(IV) is $5f^7$) decreasing by approximately 5 eV from the Cm level, so that they are nearly below the range of the ligand orbitals in energy. As briefly discussed above, this is due to Cm having a +III oxidation state, while Bk has a + IV oxidation state within their respective $[\text{An(HOPO)}]^0$ complexes. Cf and Es likewise favor the +III oxidation state, increasing the energy of the 5f orbitals in $[\text{Cf(HOPO)}]^0$ and $[\text{Es(HOPO)}]^0$ complexes, relative to Bk. The change in behavior between Cm and Bk can therefore be traced back to the oxidation state of the ion.

In their study of the f and d orbital contributions to covalency, Minasian et al. described covalent bonds using a mixing coefficient, $\lambda$, defined as

$$\lambda = \frac{H_{ML}}{|E_M^0 - E_L^0|} \tag{1}$$

where $\lambda$ ranges between zero and one depending on the degree of covalent contribution to the bond, $H_{ML}$ is the off diagonal matrix element of the Hamiltonian (proportional to the overlap integral between the two atoms making up the bond), and $E_M^0$

and $E_L^0$ are the metal and ligand orbital energies, respectively.[68] From eq 1, there are two ways in which a covalent bond can be achieved. Overlap driven covalency is realized in the presence of a significant matrix element $(H_{ML})$, indicating increased spatial overlap of orbitals. Energy degeneracy driven covalency is attained when the metal and ligand orbital energy levels are nearly degenerate; that is when the denominator $E_M^0 - E_L^0$ approaches zero. It should be noted that without a nonzero value for $H_{ML}$—at least some orbital overlap—$\lambda$ is zero and covalency of either type is not possible.

The later actinide complexes display strong energy degeneracy driven covalency as described previously by Minasian and others,[68,70,75,76] as opposed to the more traditional overlap driven covalency typical of the early actinides. Later actinide ions, which are significantly contracted relative to their earlier peers, have less spatial overlap and therefore are often thought to have primarily ionic interactions. The mixing of the 5f orbitals of later actinides with the ligand orbitals is energy degeneracy covalency in nature. Additionally, this increased orbital mixing correlates with the enhanced stability of the complexes. These results support the idea that ligand dependent energy degeneracy driven covalency is an important feature of the chemistry of the later actinides, supplanting the more traditional covalency derived from the spatial overlap of orbitals, and these results match recent calculations on the heavy actinides with dipicolinate ligands.[76] The later actinides are an ideal place to study these competing factors of covalent bonds.

## CONCLUDING REMARKS

The data presented in this study provide a thorough examination of the fundamental interactions between the HOPO ligand and actinide ions across oxidation states and solvation environments, including changes in the covalency of the actinide-ligand interactions and the ability of the ligand to oxidize or reduce ions as necessary upon complexation. Calculated structures corroborate well with experimental values, including unprecedented EXAFS data on the Am(III), Cm(III), and Cf(III) complexes. The HOPO ligand is shown to be able to both oxidize early actinide ions and reduce later actinide ions, a key to its unparalleled complexation across the series. Charge donation from the ligand occurs largely from the coordinating oxygen atoms, while charge acceptance is driven almost entirely by the pyridine ring. These properties of the HOPO ligand—which is among the strongest actinide complexing ligands known—provide insight into future ligand design. These results also highlight the importance of energy degeneracy driven covalency for the later actinides. The increase in orbital mixing between the actinide 5f orbitals and the conjugated $\pi$ orbital of the 1,2-HOPO units in the $\text{HOPO}^{4-}$ ligand as the actinide series is traversed is an important part of the chemistry of the middle and later actinides and a likely target to be exploited by future ligands designed to separate these elements.

## METHODS

**Calculations.** Structures of the metal−3,4,3-LI(1,2-HOPO) complexes were optimized using density functional theory (DFT) with the PBE functional,[77] relativistic ZORA Hamiltonian, and triple-$\zeta$ plus two polarization function (TZ2P) basis sets with the frozen core approximation applied to the inner shells $[1s^2 - 4f^{14}]$ for actinide atoms and $[1s^2]$ for C, N and O atoms.[78,79] Crystal structures for HOPO complexes have been found in two different conformers, termed A and

B for Ln complexes by Daumann et al., who determined that A is a kinetic isomer that converts into B over time, which is the more thermodynamically stable isomer based on DFT calculations.[31] Similar isomers have been observed for $Sn^{4+}$ and $Zr^{4+}$.[43,80] The more thermodynamically stable of these Ln-HOPO structures matches well with available crystal structures of An−HOPO complexes inside the protein siderocalin, which have only been found in this configuration.[32,42] These structures were used as a starting point for the DFT optimizations. Frequency calculations were performed to determine thermodynamic properties of each structure. Calculations using the hybrid PBE0 functional were used to determine thermodynamic and electronic properties. The COSMO implicit solvation model[81−84] was used to model the complexes in aqueous and protein-like environments, using a dielectric constant of 4 and a radius of 3.45 Å for the protein-like environment. All calculations were performed using ADF 2016.[85,86]

**X-ray Absorption Spectroscopy.** Solution samples of Am, Cm, and Cf complexed with HOPO were all prepared within 10 days of the synchrotron measurements and loaded into triply contained aluminum holders with kapton windows. The Am, Cm, and Cf masses were 27.1, 10.9, and 3.3 $\mu$g, respectively. The concentrations were 1.840, 0.614, and 0.207 mM. The ratio ligand/metal was 1.3 to ensure total binding of the radionuclides, and the pH was comprised between 7 and 8 (CAPS buffer).

X-ray absorption data were collected on BL 11−2 at the Stanford Synchrotron Radiation Lightsource at the Am, Cm, and Cf $L_{III}$ edges using a Si(220) double-crystal monochromator. Harmonic rejection was achieved with a Rh-coated mirror for the Am and Cm data, while the monochromator was half-tuned for the Cf data.

Data were reduced using standard procedures[87−89] using the RSXAP suite of XAFS analysis codes.[90] In particular, after a pre-edge subtraction using the Victoreen formula,[87] a 5 knot cubic spline (Am and Cm) or a fifth order Chebychev polynomial (Cf) was used to describe the embedded atom absorption $\mu_a$ when determining the EXAFS function $\chi(k) = [\mu(k) - \mu_a(k)]/\mu_a(k)$, where $\mu(k)$ is the total absorption after the pre-edge subtraction (that is, the absorption due to the element and absorption edge of interest) and $k$ is the photoelectron wave vector given by $k = [(2m_e/\hbar)(E - E_0)]^{1/2}$, where $E$ is the incident energy, $E_0$ is the photoelectron threshold energy arbitrarily defined by the energy at the half-height of the absorption edge, and $m_e$ is the rest mass of the electron.

Scattering phases and amplitudes were calculated using FEFF 10.0.1,[91] and all fits were carried out in $r$-space using RSFIT within the RSXAP suite of XAFS analysis codes.

EXAFS fit models were derived from the DFT results. It is important to note that while the DFT models were used in the calculation, the fitting methodology is only very weakly dependent on the DFT geometry, as it reduces the complicated structure to only a few pairs and models the bond length distribution with those shells without further reference to the calculated geometry.

A more complete exposition of the EXAFS methods and results is presented in the Supporting Information.

## ■ ASSOCIATED CONTENT

### Ⓢ Supporting Information

The Supporting Information is available free of charge on the ACS Publications website at DOI: 10.1021/acs.inorgchem.8b00345.

Molecular orbital diagrams, delocalization of 5f orbitals across the An series, Mulliken valence populations of An ions in complexes, spin density on HOPO groups, oxidation energy of bare ions, complexation energy in differing solvation environments, Cartesian coordinates of selected structures, EXAFS spectra, and fit results. (PDF)

## ■ AUTHOR INFORMATION

### Corresponding Authors
*(P.Y.) E-mail: pyang@lanl.gov.
*(E.R.B.) E-mail: erb@lanl.gov.

### ORCID
Morgan P. Kelley: 0000-0001-5196-9821
Jing Su: 0000-0002-6895-2150
Rebecca J. Abergel: 0000-0002-3906-8761
Enrique R. Batista: 0000-0002-3074-4022
Ping Yang: 0000-0003-4726-2860

### Notes
The authors declare no competing financial interest.

## ■ REFERENCES

(1) Whitcomb, R. C.; Ansari, A. J.; Buzzell, J. J.; McCurley, M. C.; Miller, C. W.; Smith, J. M.; Evans, D. L. A Public Health Perspective on the U.S. Response to the Fukushima Radiological Emergency. *Health Phys.* **2015**, *108* (3), 357−363.

(2) Silva, R. J.; Nitsche, H. Actinide Environmental Chemistry. *Radiochim. Acta* **1995**, *70−71* (S1), 377−396.

(3) *Management of Persons Contaminated with Radionuclides Handbook: Recommendations of the National Council on Radiation Protection and Measurements*; National Council on Radiation Protection and Measurements: Bethesda, MD, 2009.

(4) Durbin, P. W. Actinides in Animals and Man. *Chemistry of the Actinide and Transactinide Elements* **2006**, *5*, 3339−3440.

(5) Raymond, K. N.; Matzanke, B.; Müller, G. Complexation of Iron by Siderophores a Review of Their Solution and Structural Chemistry and Biological Function. *Top. Curr. Chem.* **1984**, *123*, 49−102.

(6) White, D. L.; Durbin, P. W.; Jeung, N.; Raymond, K. N. Specific Sequestering Agents for the Actinides. 16. Synthesis and Initial Biological Testing of Polydentate Oxohydroxypyridinecarboxylate Ligands. *J. Med. Chem.* **1988**, *31*, 11−18.

(7) Gorden, A. E. V.; Xu, J.; Raymond, K. N.; Durbin, P. Rational Design of Sequestering Agents for Plutonium and Other Actinides. *Chem. Rev.* **2003**, *103* (11), 4207−4282.

(8) Sturzbecher-Hoehne, M.; Deblonde, G. J. P.; Abergel, R. J. Solution Thermodynamic Evaluation of Hydroxypyridinonate Chelators 3,4,3-LI(1,2-HOPO) and 5-LIO(Me-3,2-HOPO) for UO2(VI) and Th(IV) Decorporation. *Radiochim. Acta* **2013**, *101* (6), 359−366.

(9) Sturzbecher-Hoehne, M.; Choi, T. A.; Abergel, R. J. Hydroxypyridinonate Complex Stability of Group (IV) Metals and Tetravalent F-Block Elements: The Key to the next Generation of Chelating Agents for Radiopharmaceuticals. *Inorg. Chem.* **2015**, *54* (7), 3462−3468.

(10) Sturzbecher-Hoehne, M.; Kullgren, B.; Jarvis, E. E.; An, D. D.; Abergel, R. J. Highly Luminescent and Stable Hydroxypyridinonate Complexes: A Step towards New Curium Decontamination Strategies. *Chem. - Eur. J.* **2014**, *20* (32), 9962−9968.

(11) Sturzbecher-Hoehne, M.; Ng Pak Leung, C.; D'Aléo, A.; Kullgren, B.; Prigent, A.-L.; Shuh, D. K.; Raymond, K. N.; Abergel, R. J. 3,4,3-LI(1,2-HOPO): In Vitro Formation of Highly Stable Lanthanide Complexes Translates into Efficacious in Vivo Europium Decorporation. *Dalton Trans.* **2011**, *40* (33), 8340−8346.

(12) Durbin, P. W.; Kullgren, B.; Xu, J.; Raymond, K. N. In Vivo Chelation of Am(III), Pu(IV), Np(V), and U(VI) in Mice by TREN-(Me-3,2-HOPO). *Radiat. Prot. Dosim.* **1994**, *53* (1−4), 305−309.

(13) An, D. D.; Kullgren, B.; Jarvis, E. E.; Abergel, R. J. From Early Prophylaxis to Delayed Treatment: Establishing the Plutonium Decorporation Activity Window of Hydroxypyridinonate Chelating Agents. *Chem.-Biol. Interact.* **2017**, *267*, 80−88.

(14) Xu, J.; Kullgren, B.; Durbin, P. W.; Raymond, K. N. Specific Sequestering Agents for the Actinides. 28. Synthesis and Initial Evaluation of Multidentate 4-Carbamoyl-3-Hydroxy-1-Methyl-2(1H)-Pyridinone Ligands for in Vivo plutonium(IV) Chelation. *J. Med. Chem.* **1995**, *38* (14), 2606−2614.

(15) Xu, J.; Raymond, K. N. Uranyl Sequestering Agents: Correlation of Properties and Efficacy with Structure for UO 22 + Complexes of Linear Tetradentate 1-Methyl-3-Hydroxy-2 (1H) -Pyridinone Ligands 1. *Inorg. Chem.* **1999**, *38* (20), 308−315.

(16) An, D. D.; Villalobos, J. A.; Morales-Rivera, J. A.; Rosen, C. J.; Bjornstad, K. A.; Gauny, S. S.; Choi, T. A.; Sturzbecher-Hoehne, M.; Abergel, R. J. 238Pu Elimination Profiles after Delayed Treatment with 3,4,3-LI (1,2-HOPO) in Female and Male Swiss-Webster Mice. *Int. J. Radiat. Biol.* **2014**, *90* (11), 1055−1061.

(17) Abergel, R. J.; Durbin, P. W.; Kullgren, B.; Ebbe, S. N.; Xu, J.; Chang, P. Y.; Bunin, D. I.; Blakely, E. A.; Bjornstad, K. A.; Rosen, C. J.; Shuh, D. K.; Raymond, K. N. Biomimetic Actinide Chelators: An Update on the Preclinical Development of the Orally Active Hydroxypyridonate Decorporation Agents 3,4,3-LI(1,2-HOPO) and 5-LIO(Me-3,2-HOPO). *Health Phys.* **2010**, *99* (3), 401−407.

(18) Choi, T. A.; Furimsky, A. M.; Swezey, R.; Bunin, D. I.; Byrge, P.; Iyer, L. V.; Chang, P. Y.; Abergel, R. J. In Vitro Metabolism and Stability of the Actinide Chelating Agent 3,4,3-LI(1,2-HOPO). *J. Pharm. Sci.* **2015**, *104* (5), 1832−1838.

(19) Durbin, P. W.; Kullgren, B.; Xu, J.; Raymond, K. N. Development of Decorporation Agents for the Actinides. *Radiat. Prot. Dosim.* **1998**, *79* (1−4), 433−443.

(20) Xu, J.; Churchill, D. G.; Botta, M.; Raymond, K. N. Gadolinium(III) 1,2-Hydroxypyridonate-Based Complexes: Toward MRI Contrast Agents of High Relaxivity. *Inorg. Chem.* **2004**, *43* (18), 5492−5494.

(21) Datta, A.; Raymond, K. N. Gd-Hydroxypyridinone (HOPO)-Based High-Relaxivity Magnetic Resonance Imaging (MRI) Contrast Agents. *Acc. Chem. Res.* **2009**, *42* (7), 938−947.

(22) Thompson, M. K.; Botta, M.; Nicolle, G.; Helm, L.; Aime, S.; Merbach, A. E.; Raymond, K. N. A Highly Stable Gadolinium Complex with a Fast, Associative Mechanism of Water Exchange. *J. Am. Chem. Soc.* **2003**, *125* (47), 14274−14275.

(23) Werner, E. J.; Datta, A.; Jocher, C. J.; Raymond, K. N. High-Relaxivity MRI Contrast Agents: Where Coordination Chemistry Meets Medical Imaging. *Angew. Chem., Int. Ed.* **2008**, *47* (45), 8568−8580.

(24) Captain, I.; Deblonde, G. J. P.; Rupert, P. B.; An, D. D.; Illy, M. C.; Rostan, E.; Ralston, C. Y.; Strong, R. K.; Abergel, R. J. Engineered Recognition of Tetravalent Zirconium and Thorium by Chelator-Protein Systems: Toward Flexible Radiotherapy and Imaging Platforms. *Inorg. Chem.* **2016**, *55* (22), 11930−11936.

(25) Deri, M. A.; Ponnala, S.; Zeglis, B. M.; Pohl, G.; Dannenberg, J. J.; Lewis, J. S.; Francesconi, L. C. Alternative Chelator for 89Zr Radiopharmaceuticals: Radiolabelling and Evaluatioin of 3,4,3-(LI-1,2-HOPO). *J. Med. Chem.* **2014**, *57*, 4849−4860.

(26) Daumann, L. J.; Tatum, D. S.; Andolina, C. M.; Pacold, J. I.; D'Aléo, A.; Law, G. L.; Xu, J.; Raymond, K. N. Effects of Ligand Geometry on the Photophysical Properties of Photoluminescent Eu(III) and Sm(III) 1-Hydroxypyridin-2-One Complexes in Aqueous Solution. *Inorg. Chem.* **2016**, *55* (1), 114−124.

(27) Daumann, L. J.; Werther, P.; Ziegler, M. J.; Raymond, K. N. Siderophore Inspired Tetra- and Octadentate Antenna Ligands for Luminescent Eu(III) and Tb(III) Complexes. *J. Inorg. Biochem.* **2016**, *162*, 263−273.

(28) Abergel, R. J.; D'Aleo, A.; Ng Pak Leung, C.; Shuh, D. K.; Raymond, K. N. Using the Antenna Effect as a Spectroscopic Tool: Photophysics and Solution Thermodynamics of the Model Luminescent Hydroxypyridonate Complex [Eu III(3,4,3-LI(1,2-HOPO))]-. *Inorg. Chem.* **2009**, *48* (23), 10868−10870.

(29) Agbo, P.; Xu, T.; Sturzbecher-Hoehne, M.; Abergel, R. J. Enhanced Ultraviolet Photon Capture in Ligand-Sensitized Nanocrystals. *ACS Photonics* **2016**, *3* (4), 547−552.

(30) Agbo, P.; Abergel, R. J. Ligand-Sensitized Lanthanide Nanocrystals: Merging Solid-State Photophysics and Molecular Solution Chemistry. *Inorg. Chem.* **2016**, *55* (20), 9973−9980.

(31) Daumann, L. J.; Tatum, D. S.; Snyder, B. E. R.; Ni, C.; Law, G. L.; Solomon, E. I.; Raymond, K. N. New Insights into Structure and Luminescence of EuIII and SmIII Complexes of the 3,4,3-LI(1,2-HOPO) Ligand. *J. Am. Chem. Soc.* **2015**, *137* (8), 2816−2819.

(32) Moore, E. G.; Xu, J.; Jocher, C. J.; Werner, E. J.; Raymond, K. N. Cymothoe Sangaris": An Extremely Stable and Highly Luminescent 1,2-Hydroxypyridinonate Chelate of Eu(III). *J. Am. Chem. Soc.* **2006**, *128* (33), 10648−10649.

(33) Deblonde, G. J.-P.; Sturzbecher-Hoehne, M.; Rupert, P. B.; An, D. D.; Illy, M.-C.; Ralston, C. Y.; Brabec, J.; de Jong, W. A.; Strong, R. K.; Abergel, R. J. Chelation and Stabilization of Berkelium in Oxidation State + IV. *Nat. Chem.* **2017**, *9*, 843−849.

(34) Zwier, J. M.; Bazin, H.; Lamarque, L.; Mathis, G. Luminescent Lanthanide Cryptates: From the Bench to the Bedside. *Inorg. Chem.* **2014**, *53* (4), 1854−1866.

(35) Bünzli, J.-C. G.; Eliseeva, S. V. Intriguing Aspects of Lanthanide Luminescence. *Chem. Sci.* **2013**, *4* (5), 1939−1949.

(36) Butler, S. J.; Parker, D. Anion Binding in Water at Lanthanide Centres: From Structure and Selectivity to Signalling and Sensing. *Chem. Soc. Rev.* **2013**, *42*, 1652−1666.

(37) Faulkner, S.; Pope, S. J. A.; Burton-Pye, B. P. Lanthanide Complexes for Luminescence Imaging Applications. *Appl. Spectrosc. Rev.* **2005**, *40* (1), 1−31.

(38) Wang, X.; Chang, H.; Xie, J.; Zhao, B.; Liu, B.; Xu, S.; Pei, W.; Ren, N.; Huang, L.; Huang, W. Recent Developments in Lanthanide-Based Luminescent Probes. *Coord. Chem. Rev.* **2014**, *273−274*, 201−212.

(39) Deblonde, G. J.-P.; Sturzbecher-Hoehne, M.; Abergel, R. J. Solution Thermodynamic Stability of Complexes Formed with the Octadentate Hydroxypyridinonate Ligand 3,4,3-LI(1,2-HOPO): A Critical Feature for Efficient Chelation of Lanthanide(IV) and Actinide(IV) Ions. *Inorg. Chem.* **2013**, *52*, 8805−8811.

(40) Sturzbecher-Hoehne, M.; Yang, P.; D'Aleo, A.; Abergel, R. J. Intramolecular Sensitization of Americium Luminescence in Solution: Shining Light on Short-Lived Forbidden 5f Transitions. *Dalt. Trans.* **2016**, *45*, 9912.

(41) Xu, J.; Radkov, E.; Ziegler, M.; Raymond, K. N. Plutonium (IV) Sequestration: Structural and Thermodynamic Evaluation of the Extraordinarily Stable Cerium (IV) Hydroxypyridinonate Complexes 1. *Inorg. Chem.* **2000**, *39* (Iv), 4156−4164.

(42) Allred, B. E.; Rupert, P. B.; Gauny, S. S.; An, D. D.; Ralston, C. Y.; Sturzbecher-Hoehne, M.; Strong, R. K.; Abergel, R. J. Siderocalin-Mediated Recognition, Sensitization, and Cellular Uptake of Actinides. *Proc. Natl. Acad. Sci. U. S. A.* **2015**, *112* (33), 10342−10347.

(43) Deri, M. A.; Ponnala, S.; Kozlowski, P.; Burton-Pye, B. P.; Cicek, H. T.; Hu, C.; Lewis, J. S.; Francesconi, L. C. P-SCN-Bn-HOPO: A Superior Bifunctional Chelator for 89Zr ImmunoPET. *Bioconjugate Chem.* **2015**, *26* (12), 2579−2591.

(44) Ferrier, M. G.; Batista, E. R.; Berg, J. M.; Birnbaum, E. R.; Cross, J. N.; Engle, J. W.; La Pierre, H. S.; Kozimor, S. A.; Lezama Pacheco, J. S.; Stein, B. W.; Stieber, S. C. E.; Wilson, J. J. Spectroscopic and Computational Investigation of Actinium Coordination Chemistry. *Nat. Commun.* **2016**, *7*, 12312.

(45) Schnaars, D. D.; Gaunt, A. J.; Hayton, T. W.; Jones, M. B.; Kirker, I.; Kaltsoyannis, N.; May, I.; Reilly, S. D.; Scott, B. L.; Wu, G. Bonding Trends Traversing the Tetravalent Actinide Series: Synthesis, Structural, and Computational Analysis of An IV (Ar Acnac) 4 Complexes (An = Th, U, Np, Pu; Ar Acnac = Ar N C(Ph)CHC(Ph) O; Ar = 3,5- T Bu 2 C 6 H 3. *Inorg. Chem.* **2012**, *51* (15), 8557−8566.

(46) Kaltsoyannis, N. Does Covalency Increase or Decrease across the Actinide Series? Implicartions for Minor Actinidide Partitioning. *Inorg. Chem.* **2013**, *52*, 3407−3413.

(47) Bradley, J. A.; Yang, P.; Batista, E. R.; Boland, K. S.; Burns, C. J.; Clark, D. L.; Conradson, S. D.; Kozimor, S. A.; Martin, R. L.; Seidler, G. T.; Scott, B. L.; Shuh, D. K.; Tyliszczak, T.; Wilkerson, M. P.; Wolfsberg, L. E. Experimental and Theoretical Comparison of the O K-Edge Nonresonant Inelastic X-Ray Scattering and X-Ray Absorption Spectra of NaReO₄. *J. Am. Chem. Soc.* **2010**, *132* (39), 13914−13921.

(48) Minasian, S. G.; Keith, J. M.; Batista, E. R.; Boland, K. S.; Clark, D. L.; Kozimor, S. a.; Martin, R. L.; Shuh, D. K.; Tyliszczak, T. New Evidence for 5f Covalency in Actinocenes Determined from Carbon K-Edge XAS and Electronic Structure Theory. *Chem. Sci.* **2014**, *5*, 351.

(49) Gutowski, K. E.; Dixon, D. A. Predicting the Energy of the Water Exchange Reaction and Free Energy of Solvation for the Uranyl Ion in Aqueous Solution. *J. Phys. Chem. A* **2006**, *110* (28), 8840−8856.

(50) Parmar, P.; Samuels, A.; Clark, A. E. Applications of Polarizable Continuum Models to Determine Accurate Solution-Phase Thermo-chemical Values across a Broad Range of Cation Charge - The Case of U(III-VI). *J. Chem. Theory Comput.* **2015**, *11* (1), 55−63.

(51) Kelley, M. P.; Yang, P.; Clark, S. B.; Clark, A. E. Structural and Thermodynamic Properties of the Cm III Ion Solvated by Water and Methanol. *Inorg. Chem.* **2016**, *55* (10), 4992−4999.

(52) Atta-Fynn, R.; Bylaska, E. J.; De Jong, W. a. Importance of Counteranions on the Hydration Structure of the Curium Ion. *J. Phys. Chem. Lett.* **2013**, *4* (13), 2166−2170.

(53) D'Aléo, A.; Moore, E. G.; Szigethy, G.; Xu, J.; Raymond, K. N. Aryl Bridged 1-Hydroxypyridin-2-One: Effect of the Bridge on the Eu(III) Sensitization Process. *Inorg. Chem.* **2009**, *48* (19), 9316−9324.

(54) Moore, E. G.; Xu, J.; Jocher, C. J.; Corneillie, T. M.; Raymond, K. N. Eu(III) Complexes of Functionalized Octadentate 1-Hydroxypyridin-2-Ones: Stability, Bioconjugation, and Luminescence Resonance Energy Transfer Studies. *Inorg. Chem.* **2010**, *49* (21), 9928−9939.

(55) Moore, E.; Xu, J.; Jocher, C.; Castro-Rodriguez, I.; Raymond, K. N. Highly Luminescent Lanthanide Complexes of 1-Hydroxy-2-Pyridinones. *Inorg. Chem.* **2008**, *47*, 3105−3118.

(56) Gorden, A. E. V.; Shuh, D. K.; Tiedemann, B. E. F.; Wilson, R. E.; Xu, J.; Raymond, K. N. Sequestered Plutonium: [PuIV{5LIO(Me-3,2-HOPO)}2] - The First Structurally Characterized Plutonium Hydroxypyridonate Complex. *Chem. - Eur. J.* **2005**, *11* (9), 2842−2848.

(57) Gorden, A. E. V.; Xu, J.; Szigethy, G.; Oliver, A.; Shuh, D. K.; Raymond, K. N. Characterization of a Mixed Salt of 1-Hydroxypyridin-2-One Pu (IV) Complexes. *J. Am. Chem. Soc.* **2007**, *129* (IV), 6674−6675.

(58) Riley, P. E.; Abu-dari, k.; Raymond, K. N. Specific Sequestering Agents for the Actinides. 9. Synthesis of Metal Complexes of 1-Hydroxy-2-Pyridinone and the Crystal Structure of Tetrakis(1-Oxy-2-pyridonato)aquothorium(IV) Dihydrate. *Inorg. Chem.* **1983**, *22* (2), 3940−3944.

(59) Scarrow, R. C.; Riley, P. E.; Abu-Dari, K.; White, D. L.; Raymond, K. N. NC19-Ferric Ion Sequestering Agents. 13. Synthesis, Structures, and Thermodynamics of Complexation of cobalt(III) and iron(III) Tris Complexes of Several Chelating Hydroxypyridinones. *Inorg. Chem.* **1985**, *24* (6), 954−967.

(60) Downward, L.; Booth, C. H.; Lukens, W. W.; Bridges, F. A Variation of the F-Test for Determining Statistical Relevance of Particular Parameters in EXAFS Fits. *AIP Conf. Proc.* **2006**, *882*, 129−131.

(61) Shannon, R. D. Revised Effective Ionic Radii and Systematic Studies of Interatomic Distances in Halides and Chaleogenides. *Acta Crystallogr., Sect. A: Cryst. Phys., Diffr., Theor. Gen. Crystallogr.* **1976**, *A32* (5), 751−767.

(62) Ferrier, M. G.; Stein, B. W.; Batista, E. R.; Berg, J. M.; Birnbaum, E. R.; Engle, J. W.; John, K. D.; Kozimor, S. A.; Lezama Pacheco, J. S.; Redman, L. N. Synthesis and Characterization of the Actinium Aquo Ion. *ACS Cent. Sci.* **2017**, *3* (3), 176−185.

(63) Kimura, T.; Choppin, G. R. Luminescence Study on Determination of the Hydration Number of Cm(III). *J. Alloys Compd.* **1994**, *213-214*, 313−317.

(64) Atta-fynn, R.; Bylaska, E. J.; Schenter, G. K.; de Jong, W. A. De. Hydration Shell Structure and Dynamics of Curium (III) in Aqueous Solution: First Principles and Empirical Studies. *J. Phys. Chem. A* **2011**, *115* (Iii), 4665−4677.

(65) D'Angelo, P.; Martelli, F.; Spezia, R.; Filipponi, A.; Denecke, M. A. Hydration Properties and Ionic Radii of actinide(III) Ions in Aqueous Solution. *Inorg. Chem.* **2013**, *52* (18), 10318−10324.

(66) Banik, N. L.; Vallet, V.; Réal, F.; Belmecheri, R. M.; Schimmelpfennig, B.; Rothe, J.; Marsac, R.; Lindqvist-Reis, P.; Walther, C.; Denecke, M. a; Marquardt, C. M. First Structural Characterization of Pa(IV) in Aqueous Solution and Quantum Chemical Investigations of the Tetravalent Actinides up to Bk(IV): The Evidence of a Curium Break. *Dalton Trans.* **2016**, *45* (2), 453−457.

(67) Wiebke, J.; Moritz, A.; Cao, X.; Dolg, M. Approaching actinide(+III) Hydration from First Principles. *Phys. Chem. Chem. Phys.* **2007**, *9*, 459−465.

(68) Minasian, S. G.; Keith, J. M.; Batista, E. R.; Boland, K. S.; Clark, D. L.; Conradson, S. D.; Kozimor, S. A.; Martin, R. L.; Schwarz, D. E.; Shuh, D. K.; Wagner, G. L.; Wilkerson, M. P.; Wolfsberg, L. E.; Yang, P. Determining Relative F and D Orbital Contributions to M-Cl Covalency in MCl62- (M = Ti, Zr, Hf, U) and UOCl5- Using Cl K-Edge X-Ray Absorption Spectroscopy and Time-Dependent Density Functional Theory. *J. Am. Chem. Soc.* **2012**, *134* (12), 5586−5597.

(69) Tassell, M. J.; Kaltsoyannis, N. Covalency in AnCp4 (An = Th− Cm): A Comparison of Molecular Orbital, Natural Population and Atoms-in-Molecules Analyses. *Dalt. Trans.* **2010**, *39*, 6719−6725.

(70) Prodan, I. D.; Scuseria, G. E.; Martin, R. L. Covalency in the Actinide Dioxides: Systematic Study of the Electronic Properties Using Screened Hybrid Density Functional Theory. *Phys. Rev. B: Condens. Matter Mater. Phys.* **2007**, *76* (3), 033101.

(71) Roy, L. E.; Batista, E. R.; Hay, P. J. Theoretical Studies on the Redox Potentials of Fe Dinuclear Complexes as Models for Hydrogenase. *Inorg. Chem.* **2008**, *47* (20), 9228−9237.

(72) Liu, J.-B.; Chen, G. P.; Huang, W.; Clark, D. L.; Schwarz, W. H. E.; Li, J. Bonding Trends across the Series of Tricarbonato-Actinyl Anions [(AnO 2)(CO 3) 3] 4− (An = U−Cm): The Plutonium Turn. *Dalt. Trans.* **2017**, *46* (8), 2542−2550.

(73) Huang, W.; Jiang, N.; Schwarz, W. H. E.; Yang, P.; Li, J. Diversity of Chemical Bonding and Oxidation States in MS4Molecules of Group 8 Elements. *Chem. - Eur. J.* **2017**, *23* (44), 10580−10589.

(74) Bursten, E.; Rhodes, F.; Strittmatter, J. The Bonding in Tris(n⁵-Cyclopentadienyl Actinide Complexes IV: Electronic Structure Effects in AnCl₃ and (n⁵-C₅H₅)₃An (An = Th-Cf) Complexes. *J. Less-Common Met.* **1989**, *149*, 207−211.

(75) Neidig, M. L.; Clark, D. L.; Martin, R. L. Covalency in F-Element Complexes. *Coord. Chem. Rev.* **2013**, *257* (2), 394−406.

(76) Kelley, M. P.; Su, J.; Urban, M.; Luckey, M.; Batista, E. R.; Yang, P.; Shafer, J. C. On the Origin of Covalent Bonding in Heavy Actinides. *J. Am. Chem. Soc.* **2017**, *139*, 9901−9908.

(77) Perdew, J. P.; Burke, K.; Ernzerhof, M. Generalized Gradient Approximation Made Simple. *Phys. Rev. Lett.* **1996**, *77* (18), 3865−3868.

(78) Cao, X.; Dolg, M.; Stoll, H. Valence Basis Sets for Relativistic Energy-Consistent Small-Core Actinide Pseudopotentials. *J. Chem. Phys.* **2003**, *118* (2), 487−496.

(79) Kuchle, W.; Dolg, M.; Stoll, H.; Preuss, H. Energy-Adjusted Pseudopotentials for the Actinides. Parameter Sets and Test Calculations for Thorium and Thorium Monoxide. *J. Chem. Phys.* **1994**, *100* (10), 7535−7542.

(80) Deblonde, G. J.-P.; Lohrey, T. D.; An, D. D.; Abergel, R. J. Toxic Heavy Metal − Pb, Cd, Sn − Complexation by the Octadentate Hydroxypyridinonate Ligand Archetype 3,4,3-LI(1,2-HOPO). *New J. Chem.* **2018**, DOI: 10.1039/C7NJ04559J.

(81) Klamt, A.; Schuurmann, G. COSMO: A New Approach to Dielectric Screening in Solvents with Explicit Expressions for the Screening Energy and Its Gradient. *J. Chem. Soc., Perkin Trans. 2* **1993**, *2*, 799.

(82) Klamt, A. Conductor-like Screening Model for Real Solvents: A New Approach to the Quantitative Calculation of Solvation Phenomena. *J. Phys. Chem.* **1995**, *99* (7), 2224−2235.

(83) Klamt, A.; Jonas, V. Treatment of the Outlying Charge in Continuum Solvation Models. *J. Chem. Phys.* **1996**, *105* (May), 9972−9981.

(84) Pye, C. C.; Ziegler, T. An Implementation of the Conductor-like Screening Model of Solvation within the Amsterdam Density Functional Package. *Theor. Chem. Acc.* **1999**, *101*, 396−408.

(85) Te Velde, G.; Bickelhaupt, F. M.; Baerends, E. J.; Fonseca Guerra, C.; van Gisbergen, S. J. a.; Snijders, J. G.; Ziegler, T. Chemistry with ADF. *J. Comput. Chem.* **2001**, *22* (9), 931−967.

(86) Fonseca Guerra, F. C.; Snijders, J. G.; Te Velde, G.; Baerends, E. J. Towards an Order- N DFT Method. *Theor. Chem. Acc.* **1998**, *99* (6), 391−403.

(87) Li, G. G.; Bridges, F.; Booth, C. H. X-Ray-Absorption Fine-Structure Standards: A Comparison of Experiment and Theory. *Phys. Rev. B: Condens. Matter Mater. Phys.* **1995**, *52* (9), 6332−6348.

(88) Hayes, T. M.; Boyce, J. B. EXAFS Spectroscopy. *Solid State Phys.* **1983**, *37*, 173.

(89) Booth, C. H.; Hu, Y.-J. Confirmation of Standard Error Analysis Techniques Applied to EXAFS Using Simulations. *J. Phys. Conf. Ser.* **2009**, *190*, 012028.

(90) Booth, C. H. RSXAP Analysis Package. http://lise.lbl.gov/RSXAP/ 2016.

(91) Rehr, J. J.; Kas, J. J.; Vila, F. D.; Prange, M. P.; Jorissen, K. Parameter-Free Calculations of X-Ray Spectra with FEFF9. *Phys. Chem. Chem. Phys.* **2010**, *12* (21), 5503−5513.